Analysis of PIV images of transonic buffet flow by recurrent deep learning based optical flow prediction

C. Lagemann[1,*], E. Mäteling[1], M. Klaas[1], W. Schröder[1]

1: Chair of Fluid Mechanics and Institute of Aerodynamics, RWTH Aachen University, Germany
*Corresponding author: c.lagemann@aia.rwth-aachen.de

Keywords: PIV processing, Deep learning, Recurrent neural networks, Transonic buffet

ABSTRACT

In the past few years, several algorithms have been proposed that leverage deep learning techniques within the data analysis workflow of particle-image velocimetry (PIV) experiments. This emerging body of work has shown that deep learning has the potential to match or outperform state-of-the-art classical algorithms in terms of efficiency, accuracy, and spatial resolution. Due to the significant relevance of PIV experiments in the broader fluid mechanics community, progress in PIV processing approaches based on state-of-the-art machine learning tools has a major impact across a range of problems in applied physics and engineering where velocity components of flow fields need to be determined. In contrast to existing methods, these approaches are general, near-automated and yield per-pixel flow estimates. Primary work on deep learning for PIV is promising, but important questions concerning the application to challenging engineering problems remain open and more scientific analyses are necessary to substantiate the general confidence amongst practitioners in such neural network based tools. This motivates us to employ a novel deep learning based PIV approach called RAFT-PIV (Lagemann et al., 2021) to a challenging real-world application of a recent research subject. That is, we use our neural optical flow approach to evaluate Background-Oriented Schlieren (BOS) and PIV images obtained by measurements of the transonic flow around a supercritical DRA-2303 profile and demonstrate that it can be used as a direct one-to-one replacement for standard cross-correlation based counterparts.

1. Introduction

Within the transonic flight regime, transonic buffet might be induced by a shock-boundary layer interaction and the corresponding flow separation on the upper wing surface. The resulting pressure distribution yields unsteady loads which are acting on the wing structure while its aeroelastic response, the so-called buffeting, might lead to a structural fatigue of the wing or even fatal material failure. Therefore, transonic buffet is still of considerable research interest in the aviation industry and the underlying mechanisms sustaining the shock wave oscillations during buffet are not fully understood. However, a detailed understanding of the underlying physics is necessary to develop precise prediction methods for the onset of buffet, to shift the buffet boundary to higher

Mach numbers or angles of attack, and to find strategies to damp or even suppress buffet, which will enhance the operational performance of an aircraft.

Transonic buffet is a low frequency/ large amplitude shock wave oscillation occurring within a certain range of Mach numbers and angles of attack. Existing theories and models explaining the origin of buffet are still discussed controversially. They are primarily tailored to specific airfoils and flow conditions. For supercritical airfoils, a widely recognized buffet description has been given by Lee (1990) proposing a self-sustained feedback loop in which disturbances created at the shock foot propagate downstream within the boundary layer and generate pressure waves while passing over the trailing edge. These pressure waves travel upstream and interact with the shock wave to enhance its oscillatory motion. Numerical and experimental results of Xiao et al. (2006), Deck (2005), Hartmann et al. (2012), Hartmann, Feldhusen, & Schröder (2013), Hartmann, Klaas, & Schröder (2013), D'Aguanno et al. (2019b), D'Aguanno et al. (2019a), and D'Aguanno et al. (2021a) agree well with Lee's theory.

A different theory targeting the onset of transonic buffet was proposed by Crouch et al. (2009) based on a global stability analysis of several unsteady Reynolds-averaged Navier Stokes (URANS) simulations of a symmetrical NACA 0012 profile for varying freestream Mach numbers and angles of attack, and a chord-based Reynolds number of $Re_c = 10^7$. They identified a strong link between buffet onset and the appearance of an unstable global mode and showed that a critical angle of attack exists for a given Mach number above which transonic buffet occurs. Moreover, the shape of the fluctuating streamwise velocity component of the unstable mode shows a coupled movement of the shock wave and the boundary layer downstream of the shock wave.

Sartor et al. (2015) employed global stability, adjoint, and resolvent analysis to examine transonic buffet flow around a NACA 0012 airfoil at $Re_c = 3 \times 10^6$ and argued that buffet can be considered to be the only global instability in the flow field. Essentially, it is shown that the origin of the shock unsteadiness is located at the shock foot on the suction side of the airfoil. Furthermore, a singular-value decomposition of the global resolvent revealed that, besides the shock unsteadiness, further medium-frequency and broadband instabilities occur, which are linked to Kelvin-Helmholtz instabilities in the separation and trailing edge region. Similarly, Kojima et al. (2020) performed a resolvent analysis to identify the origin of transonic buffet for a low Reynolds number flow around a NACA 0012 airfoil. The source of buffet is identified to be at the shock foot and it is shown that the amplification mechanism of buffet is already present in low Reynolds number conditions. Pertubations within the boundary layer at the shock foot can be amplified to create shock oscillations at the characteristic buffet frequency. They also noted that these pertubations are closely linked to changes in the flow around the trailing edge explaining the effectiveness of trailing edge buffet control devices.

This discussion regarding the onset and the role of acoustic waves in the self-sustained mechanism of transonic buffet motivates the present study. That is, we particularly focus on the effect of artificial sound waves on transonic buffet to shed some light on the significance of upstream traveling pressure waves and their respective participation within the self-sustained shock oscillation. We perform extensive PIV and BOS measurements simultaneously for a reference configuration at dif-

ferent Mach numbers and for a test case with artificial sound waves originating from a resonating horn cavity. The applied image-based methods are key techniques in modern experimental fluid mechanics used to determine the velocity components and density gradients of flow fields in a wide range of complex engineering problems.
However, current processing tools usually compute the most probable particle displacement of the captured particle images based on the cross-correlation between corresponding interrogation windows. This, in fact, always yields a spatially averaged optical flow output since a single displacement vector is estimated for an entire interrogation window. Especially in PIV experiments, the state-of-the-art additionally uses a wide range of other elements including subpixel interpolation, multigrid correlation schemes, automatic outlier detection, and window deformation according to local velocity gradients. Usually, these approaches fully compensate for the loss-of-correlation due to in-plane motion if the flow within the final interrogation window is homogeneous or linearly varying. However, if the displacement is more complex due to unresolved fluctuations, non-constant velocity gradients, or out-of-plane displacement, the correlation peak is broadened and its intensity is reduced. Thus, the estimated mean field matches the ground truth fairly well, but velocity fluctuations are usually underestimated. A similar bias error can be observed in cases of inhomogeneously distributed tracer particles which is typical for near-wall flows.

In the past few years, several algorithms have been proposed that leverage deep learning techniques within the data analysis workflow of PIV experiments. This emerging field has shown that deep learning has the potential to match or outperform state-of-the-art classical algorithms in terms of efficiency, accuracy, and spatial resolution. In contrast to existing methods, these approaches are general, near-automated and yield per-pixel flow estimates. These methods circumvent the problem of manually designing an analytical pipeline by defining an end-to-end network whose output is the dense per-pixel optical flow field. Thus, fine flow structures can be resolved which alternatively are smoothed due to the spatial averaging inherent to traditional cross-correlation based methods. One promising approach is a deep learning based method inspired by the recently famous RAFT (Teed & Deng, 2020) backbone. RAFT-PIV (Lagemann et al., 2021) is a neural optical flow estimator which is specifically designed for the use case of PIV images. It operates entirely on a specific input resolution and updates iteratively its flow predictions. In the methodological paper (Lagemann et al., 2021), RAFT-PIV was shown to achieve a new state-of-the-art accuracy on a public PIV database and to outperform available supervised and unsupervised learning based approaches by a large margin. Its tremendous success based on a superior generalization ability was demonstrated for a series of different datasets that allow robust conclusions to be drawn on the utility of deep learning for PIV analysis (). However, there is still a general lack of confidence in novel deep learning based processing methods within a majority of the experimental fluids community.

Hence, the objective of the present work ultimately is twofold: (1) to evidence the generalization and usefulness of our neural RAFT-PIV approach in challenging real-world applications to

enhance the general confidence in neural processing approaches amongst practitioners, and (2) to shed some light on the significance of upstream traveling pressure waves and their respective participation within the self-sustained shock oscillation of transonic buffet. Moreover, we discuss some interesting test cases in which we observe a strong buffet excitation by means of cavity noise.

2. Experimental setup

The experimental investigations were conducted in the Trisonic Wind Tunnel of the Institute of Aerodynamics. This facility is an intermittently working vacuum storage tunnel reaching Mach numbers from 0.4 to 3.0. A silica gel based drier keeps the relative humidity of the air well below 4% at a total temperature of about $293\ K$ to exclude any influence on the shock-wave position (Hartmann, Feldhusen, & Schröder, 2013). The dried air is stored in the balloon of the tunnel prior to the test run. Depending on the Mach number, the entire test run lasts about 10 seconds with $2-3$ seconds of stable flow conditions at a turbulence intensity less than 1%. The total pressure and temperature of the wind tunnel are determined by the ambient conditions. Therefore, the Reynolds number depends on the Mach number and the ambient temperature and is set to $Re_c \approx 2.1 \cdot 10^6$ in the present experiments.
At transonic flows, the tunnel is equipped with a $0.4m \times 0.4m$ two-dimensional adaptive test section consisting of parallel side walls and flexible upper and lower walls to simulate unconfined flow conditions (Hartmann et al., 2012). The wall contours are calculated a-priori solving the Cauchy integral based on the time-averaged pressure distribution. Since the resulting wall contours are time-averaged, the time-resolved wall pressure distribution is also measured by 26 dynamic pressure transducers distributed along the centerline of the upper and lower wall.

The rigid airfoil model is the supercritical profile DRA 2303, which was previously investigated in Hartmann et al. (2012), Hartmann, Feldhusen, & Schröder (2013) and Feldhusen-Hoffmann et al. (2018). The airfoil has a relative thickness to chord ratio of 14% and a chord length of $c = 150mm$. The airfoil model is made of stainless steel and a $117\mu m$ zigzag shaped transition strip is fixed at 5% chord to trigger the laminar-turbulent transition of the boundary layer. To obtain valid reference data, all measurements are conducted without any external perturbations first, referred to as REF in the following, followed by experiments with an acoustic excitation.

To investigate the effect of artificially introduced sound waves on the flow characteristics, we conducted planar PIV and BOS measurements simultaneously. A sketch of the experimental setup is given in Fig. 1. The laser light sheet of the PIV measurement is positioned parallel to the incoming flow ranging $0.35 < x/c < 1.3$ on the test section center line. Droplets of Di-Ethyl-Hexyl-Sebacat (DEHS) are used as seeding, which are filtered using a cyclone particle separator to achieve a mean diameter of $0.6\mu m$. To ensure a homogenous particle distribution, the seeding is added to the flow in the dry air reservoir of the wind tunnel prior to each test run. The flow was illuminated using a Quantronix Darwin Duo 100 double-pulsed Nd:YLF laser with a wavelength of $527nm$. The thickness of the laser light sheet is approximately $1mm$. The laser pulse separation in the exper-

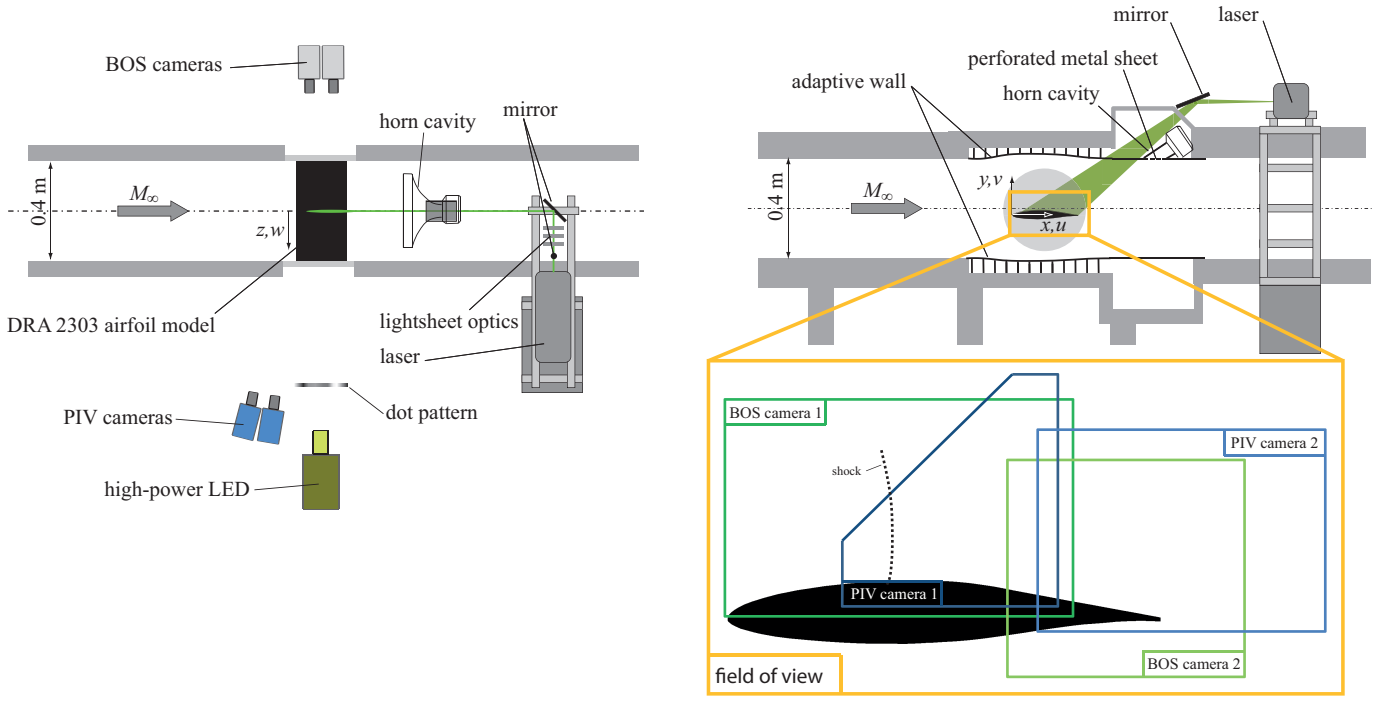

Figure 1. Experimental setup of simultaneous PIV and BOS measurements: Top view (left); side view (right) augmented by a zoom-in to illustrate the individual FOV of each camera.

iments is $\Delta t = 4.0\mu s$ leading to a mean particle displacement of approximately 10 pixels in the subsonic flow areas. Particle images are recorded by two pco.dimax HS4 which are mounted at a small angle to the normal of the light sheet under Scheimpflug condition to ensure optical access for the simultaneous BOS measurements. Both cameras are equipped with a $100mm$ Zeiss macro lens at an aperture of $f/2.0$ to realize a field of view (FOV) of $60mm \times 150mm$ in the measurement plane (FOV of a single camera: $\approx 60mm \times 85mm$, see Figure 1). Each measurement consists of 2000 double images recorded over a measurement time of $0.5s$ ($f_{PIV} = 4000\ Hz$) corresponding to approximately 85 Buffet cycles. First, to remove the background in the particle images, a sliding background is subtracted from the particle images. The sliding background is calculated for every laser cavity separately using an iterative procedure. First, the mean and the standard deviation of the image brightness is calculated over a span of 31 images for every pixel. In the following four iterations, values that deviate from the mean by more than 1.5 times the standard deviation are excluded from the statistics. Hence, pixels that contain particles are excluded from the statistics and a much shorter span is sufficient to generate a convincing background image. After the background subtraction, the particle images are preprocessed using a non-linear Gaussian blur to reduce camera noise and are dewarped using a camera calibration based on the Tsai model (Tsai, 1987). For the camera calibration, a CNC (Computerized Numerical Control) machined aluminum target with $0.2mm$ holes filled with black paint with a spacing of $1.5mm$ is used. Therefore, approx. 2000 calibration points are used for the calibration of each camera.

To measure density gradients, we conducted BOS measurements simultaneously using a second

camera setup. A shown in Figure 1, a random point pattern was installed in the background (dot size: $\approx 0.3mm$ in diameter corresponding to approx. $2\,px$, dot density: $\approx 1.6dots/mm$) illuminated by a single high-power LED. Two Photron Fastcam SA5 are used to record the background pattern, each equipped with a $180mm$ Tamron tele macro lens at an aperture of $f/5.6$. Each measurement consists of 4000 snapshots recorded over a measurement time of $0.5s$ resulting in a doubled sampling frequency compared to the PIV measurements ($f_{BOS} = 8000\ Hz$) since we were highly interested in resolving upstream traveling waves. A similar image processing scheme as described above (final window size $16 \times 16px^2$, overlap 75%) was used to estimate the density gradients with respect to the calibration image resulting in a validation rate over 95%.
Throughout this manuscript, the x-coordinate and the streamwise velocity component u point in the horizontal and the y-coordinate and the normal velocity component v in the vertical direction as given in Fig. 1.

3. Methods

3.1. RAFT-PIV

In the following, the most important architectural aspects of RAFT-PIV are presented based on introduction in the original methodological paper (Lagemann et al., 2021). RAFT-PIV is a neural optical flow estimator which is specifically designed for the use case of PIV images and is based on the successful RAFT architecture (Teed & Deng, 2020). It is unique in the sense that it operates entirely on a specific input resolution and updates iteratively its flow predictions. RAFT-PIV was shown to achieve a new state-of-the-art accuracy on a public PIV database and to outperform available supervised and unsupervised learning based approaches by a large margin.

RAFT-PIV mainly consists of three stages, a feature extracting block, the computation of a full correlation volume between all pairs, and iterative updates based on a convolutional Gated Recurrent Unit (ConvGRU), as shown in Fig. 2.

In a first step (Fig. 2 (I)), features are extracted from the two input images $\mathbf{I}_1$ and $\mathbf{I}_2$ in a shared feature encoder. It mainly consists of three different CNN modules each containing two residual blocks that map the particle image input to dense feature maps. These high-dimensional feature embeddings are a rich representation of the input images derived from input image feature like edges or textures.
A second network, the context network, extracts valuable context features from the first image (Fig. 2 (III)). The context network is required since the correlation volume expresses similarities between pairs of features, but is not intended to connect dominant correlation patterns to specific image features. The feature extraction and the context network form the first stage of the RAFT backbone.

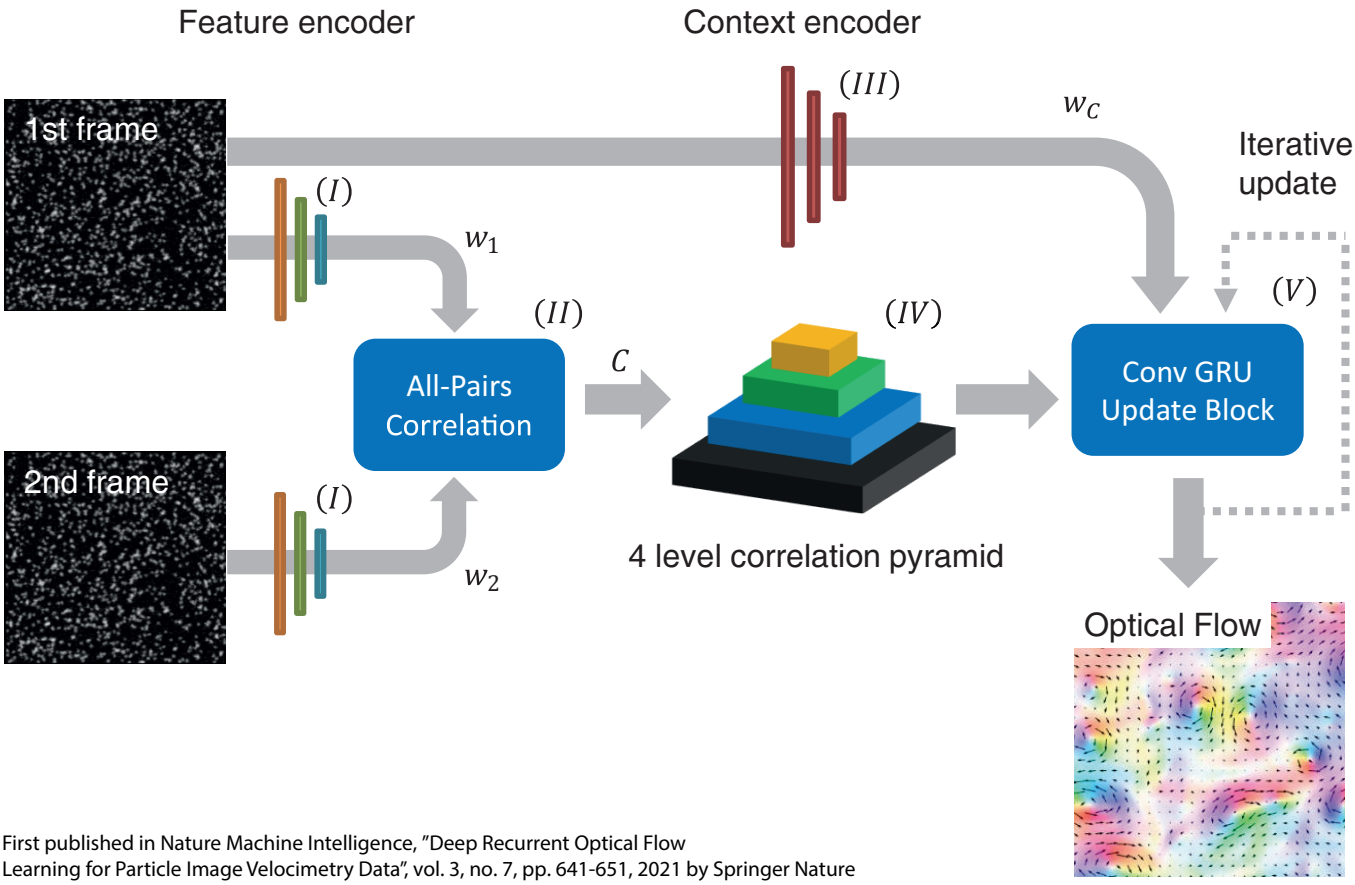

Figure 2. Main components of RAFT-PIV comprising a shared feature encoder (I), the context encoder using the same topology as the feature encoder (III), an All-Pairs correlation layer (II), a correlation pyramid (IV), and the update operator (V) which recurrently updates the optical flow estimates using a convolutional GRU (from (Lagemann et al., 2021)).

The second stage of RAFT-PIV (Fig. 2 (II)) is designed such that it computes the similarity of both image feature maps $\mathbf{F}_1$ and $\mathbf{F}_2$ using a full correlation volume between all pairs of both feature maps. The similarity between two pixel embeddings $(\mathbf{F}_{i,j}, \mathbf{F}_{k,l})$ is measured by the dot product between the two individual feature vectors which finally yields the so-called correlation volume

$$\mathbf{C}_{ijkl} = \sum_{D} (\mathbf{F}_1)_{ijD} \cdot (\mathbf{F}_2)_{klD} \tag{1}$$

with i, j denoting pixel coordinates in image $\mathbf{I}_1$ and k, l in image $\mathbf{I}_2$. D is the channel dimension of the feature matrix. In this context, all-pairs correlation means that every pixel is correlated with every other pixel. Hence, $\mathbf{C}(i, j, :, :)$ represents a correlation map of pixel (i, j) in $\mathbf{I}_1$ with all pixels of the second image $\mathbf{I}_2$. In comparison to a cross-correlation used in common PIV algorithms, two key differences arise: First, RAFT-PIV uses the dot product of two high-dimensional inputs and second, the pixel embeddings stem from learnable non-linear projections mapping each pixel and its neighbourhood to a high-dimensional embedding space.

Subsequently, a 4-layer correlation pyramid is formed by pooling the last two dimensions sequentially from level to level while using kernel sizes and strides of 1, 2, 4, 8 (Fig. 2 (IV)). Thus, RAFT-

PIV maintains high resolution information of the first image $\mathbf{I}_1$, while effectively addressing large object displacement applying pooling operations along the features of the second image.

During the final stage (Fig. 2(V)), the estimated flow field is updated using a ConvGRU (Siam et al., 2017). A ConvGRU is a type of recurrent neural network that stores hidden state information of previous steps to modulate a limited content memory. Thus, observation of previous steps are taken into account when estimating future predictions. The applied ConvGRU takes flow, correlation, and the hidden state of the context network as input and yields a new hidden state $\mathbf{h}_t$. Subsequently, $\mathbf{h}_t$ is passed through two convolutional layers and finally outputs the flow update $\Delta\mathbf{V}$. Thus, the final flow prediction is a combination of the sequence of residual flow updates. The benefit of a ConvGRU to perform the iterative refinement lies in the reduction of the search space due to its recurrent nature.

3.2. Standard cross-correlation based benchmark

The proposed RAFT-PIV approach is benchmarked against a high-performance in-house code called PascalPIV (Marquardt et al., 2019) which represents the current gold-standard of PIV algorithms. To allow particle shifts larger than half the interrogation window size, the image evaluation uses a multigrid approach with integer window shift to get an initial displacement field. The velocity field is refined using an iterative predictor–corrector scheme with subpixel accurate image deformation according to the procedure described by Astarita & Cardone (2005). The initial displacement is interpolated for each pixel of the image using a third-order B-spline interpolation. Both images are then deformed by half the displacement to get a second-order-accurate estimation of the displacement field. The image interpolation uses Lanczos resampling ,i.e., Lanczos windowed cardinal sine interpolation, incorporating the neighboring $8 \times 8px^2$. An integral velocity predictor is used to ensure convergence of the iterative scheme (Scarano, 2004). Hence, the predictor is the weighted average of the per-pixel displacement over the interrogation window. The corrector is determined by evaluating the cross-correlation function between both exposures with a 3-point Gaussian peak estimator (Raffel et al., 2018). The initial window size for the multigrid evaluation is $128 \times 128px^2$ and the window size used for the iterative PIV evaluation is $32 \times 32px^2$ with 75% overlap. This leads to a final vector spacing of $0.667mm$. Between the iterations, outliers in the vector field are detected using a normalized median test (Westerweel & Scarano, 2005) and replaced by interpolated values. A total of three multigrid steps and five steps of the iterative evaluation are performed, resulting in a validation rate over 90% in the final data set.

3.3. Noise-Assisted Multivariate Empirical Mode Decomposition

The EMD is a data-driven decomposition method that was pioneered by Huang et al. (1998) to analyze non-linear and unsteady temporal data in a physically meaningful manner. The resulting Intrinsic Mode Functions (IMFs) are solely based on the characteristic time scales inherent to the

data. Thus, the modes are adaptively biased towards locally dominant frequencies, which enables the extraction of physically relevant unsteady processes in a finite bandwidth.
To tackle the problems of uniqueness, mode mixing, and mode alignment, a multivariate EMD (MEMD) approach for time-dependent data was introduced by Rehman & Mandic (2010). It enables a scale alignment across multiple signals by a simultaneous decomposition of the former. To further improve frequency localization and to reduce mode mixing, Rehman & Mandic (2011) and Rehman et al. (2013) established the noise-assisted MEMD (NA-MEMD). By decomposing the multivariate data with additional variates of pure Gaussian noise, the resulting IMFs are normally distributed and possess identical Fourier spectra with doubled mean periods of neighbouring modes. In the current application, a 2D NA-MEMD Mäteling & Schröder (2022) is used in a spatial-temporal framework to precisely extract the shock within the BOS data. In this context, different variates reflect different time steps to ensure a temporal coherence between the extracted spatial shock profiles.
In the following, the steps involved in the 2D NA-MEMD algorithm are briefly discussed. Further details can be found in Mäteling & Schröder (2022).

1. Determination of direction vectors d^{φ_k} using a low-discrepancy pointset (here, the Hammersley sequence) for uniformly sampling on an $(n-1)$ unit sphere, where $k = [1, K]$ denotes the projection directions with the total number K, φ_k represents the angle corresponding to each point on the unit sphere, and n is the total number of variates including the additional noise-containing variates.
2. Projection of the multivariate input signal g along all direction vectors d^{φ_k}, which yields a set of projections p^{φ_k}.
3. Determination of the time instants $\{t_i^{\varphi_k}\}$ of the extrema of the projected signals.
4. Interpolation of the original data g at $\{t_i^{\varphi_k}\}$ to obtain the multivariate envelopes $E_{min}^{\varphi_k}$ using the minima and $E_{max}^{\varphi_k}$ using the maxima locations.
5. Calculation of the mean envelope $m = \dfrac{1}{2K}\displaystyle\sum_{k=1}^{K}(E_{min}^{\varphi_k} + E_{max}^{\varphi_k})$.
6. Determination of the detail $D = g - m$. If D fulfills the stopping criterion, it is the first IMF and the above procedure is applied to $g - D$ to obtain the subsequent IMFs. Otherwise, the procedure is applied to D until the newly obtained D satisfies the stopping criterion. Details on the stopping criterion are given in Mäteling & Schröder (2022).

In the current analysis, two additional noise channels are used and the standard deviation of the Gaussian noise possesses 2 % of the standard deviation of the multivariate data. The default values for the stopping criterion given by Rehman & Mandic (2010) are applied and the decomposition is based on $K = 22$ projection directions.

4. Results

4.1. Comparison of deep learning and cross-correlation PIV algorithms

To demonstrate that RAFT-PIV serves as a direct one-to-one replacement of classical cross-correlation based algorithms and is applicable in common research topics, the findings of this study ultimately build upon the inference runs of RAFT-PIV applied to BOS and PIV images dealing with a transonic flow around the supercritical DRA-2303 airfoil. Note that the present image conditions are essentially far from being perfect for two reason: First, reflections on the airfoil surface impede a precise displacement prediction close to the surface. Second, the signal-to-noise ratio (SNR) of this dataset is comparably low. Due to the high-speed PIV measurements ($f_{PIV} = 4000Hz$) and the comparably small pulse-to-pulse distance, only a fraction of the laser power is accessible. Nonetheless, Fig. 3 exhibits good results of RAFT-PIV under these challenging conditions and evidences the generalization ability of the proposed neural PIV tool. The predicted velocity fields match closely the results of the high-performance in-house code PascalPIV while the output resolution is substantially increased. Thus, the estimated velocity fields appear in greater detail and contain

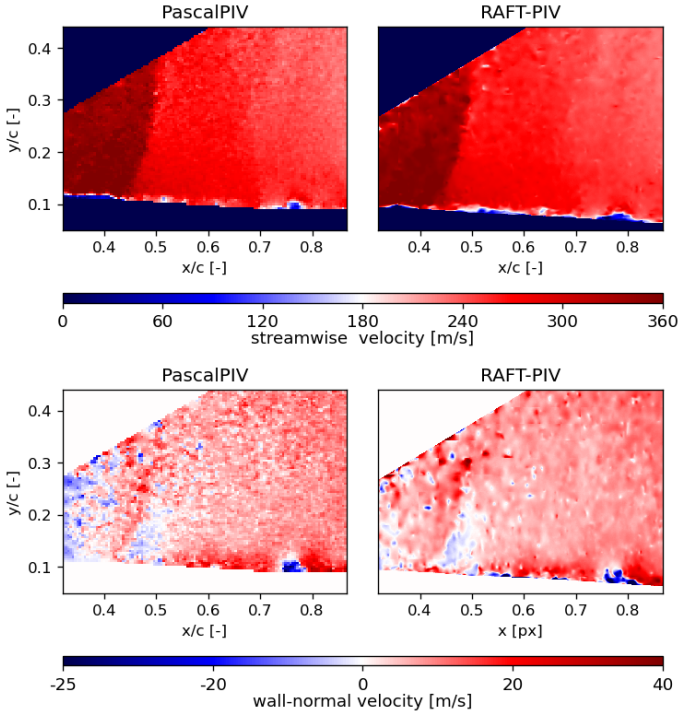

(a) First PIV camera

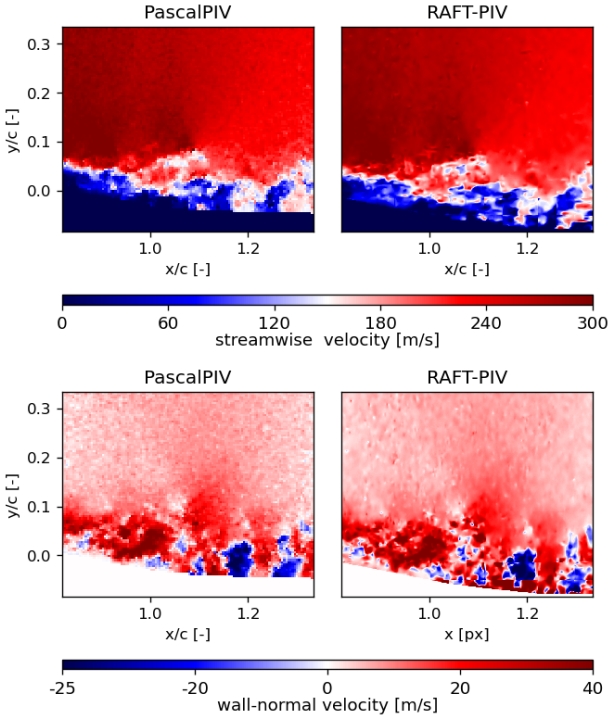

(b) Second PIV camera

Figure 3. Comparison of exemplary evaluation results of the neural PIV-processing tool RAFT-PIV and the classical cross-correlation based PascalPIV

smaller flow structures. It is remarkable that even physical singularities like the shock wave are predicted correctly although such flows are not addressed in the training dataset.
Further evidence for the great generalization ability of RAFT-PIV and its usefulness in general image based fluid measurements is derived by its application to the BOS image data. Although the

measurement principle and the fluid quantities are fundamentally different from the original PIV application, the image processing tasks bear a deep resemblance and enables us to use RAFT-PIV for evaluation. Fig. 4 shows a side-by-side comparison of the PascalPIV benchmark and RAFT-PIV results applied to the BOS data. Although the image feature distribution of the background dot pattern was not addressed in the training particle image dataset, a supervised RAFT-PIV model extracts precisely all relevant density gradients. Note that the discontinuities of the airfoil shape emanate from local glass damages in the sidewalls of the windtunnel. It is even more remarkable that the noise level of the neural optical flow algorithm is noticeably lower compared to PascalPIV while an overall smooth displacement field is estimated with distinct edges at the shock boundaries.

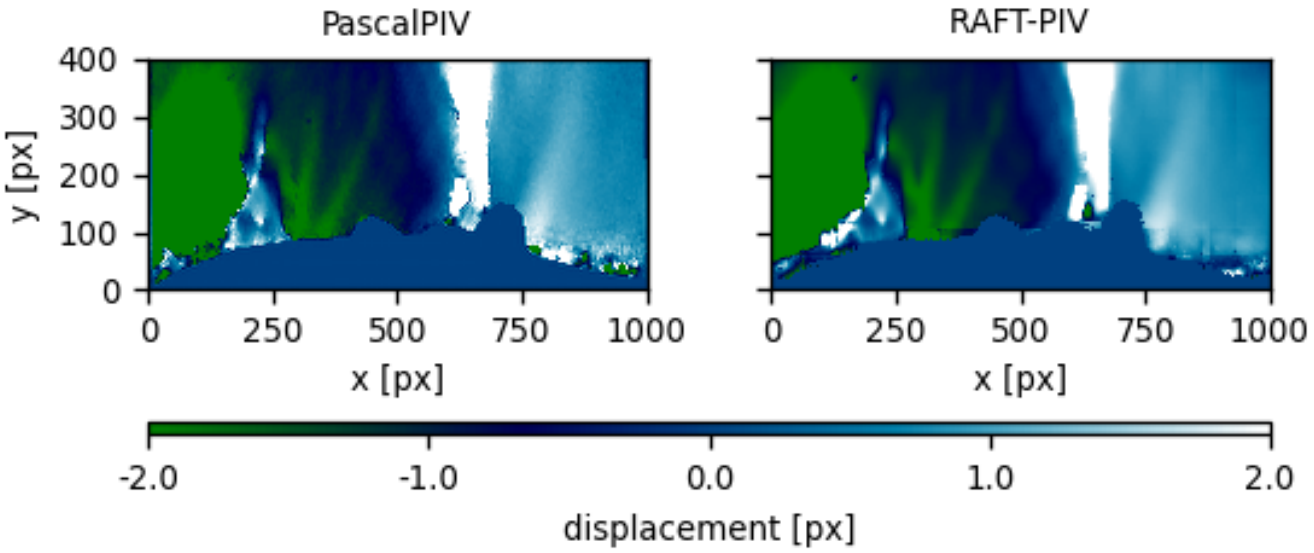

Figure 4. Comparison of exemplary evaluation results of the neural PIV-processing tool RAFT-PIV and the classical cross-correlation based counterpart PascalPIV for a set BOS images

Fig. 5 further highlights that also subsequent analysis of the displacement fields obtained by our neural optical flow estimator derives equal conclusions compared to a cross-correlation based counterpart. That is, the instantaneous shock position as well as its corresponding FFT power spectra are very close to the initial findings of the established PIV tool and evidence that not only single image frames, but the entire data sequence is evaluated precisely by RAFT-PIV. Hence, we continue to provide findings which are derived exclusively by inference runs of the RAFT-PIV algorithm in the following. Further examples demonstrating the generalization of RAFT-PIV can be found in Lagemann et al. (2022).

4.2. Transonic buffet characteristics of the reference case

In the following, the characteristic flow features of transonic buffet for the reference case are briefly described. That is, we subsequently increase the Mach number ranging from pre-buffet flow at

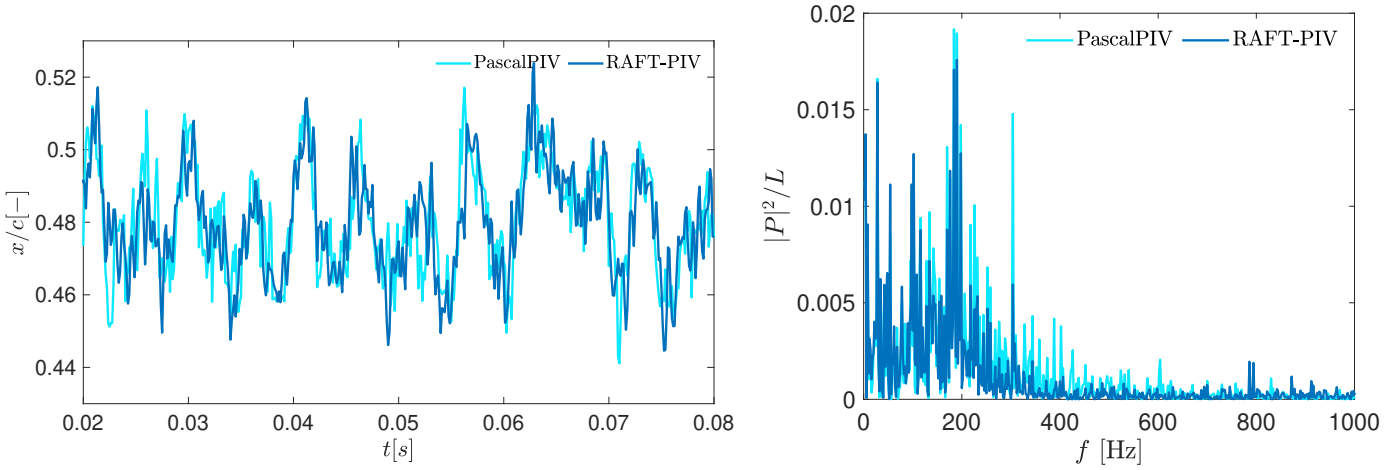

(a) Temporal extract of the instantaneous shock position

(b) Power spectra of the FFT applied to the instantaneous shock position

Figure 5. Temporal extract and FFT based power spectra of the instantaneous shock position applied to the reference case at $Ma = 0.76$ for the cross-correlation based algorithm PascalPIV and the neural RAFT-PIV

$Ma = 0.68$ to fully developed buffet conditions at $Ma = 0.76$. Since the FOV of our PIV measurements merely captures the lower half of the shock due to constraints in the optical access, a spatial 2D NA-MEMD is applied to the BOS data to capture the instantaneous shock position (see Fig. 1 depicting the specific FOVs of each camera). This has the additional advantage of a doubled temporal resolution of the shock movement compared to PIV data. To ensure a temporal coherence between the extracted shock profiles, different variates correspond to consecutive time steps. The instantaneous shock position can then be extracted from the first IMF as it contains distinct boundaries of the shock wave. Then, a mean shock position for each time step is obtained by a weighted average over all streamwise positions enclosed by the shock boundaries.

An extract of the resulting temporal evolution of the shock position, normalized by the chord length, for $Ma \geq 0.72$ is shown in Fig. 6a. Note that low Ma number configurations, i.e., $Ma \leq 0.70$, do not develop a distinct shock wave and are rather characterized by a system of multiple weak shocks making it impossible to track a distinct shock position. Hence, the first pre-buffet configuration comprising a distinct, single shock wave occurs at $Ma = 0.72$. In this case, the shock wave starts to oscillate slightly while the mean shock position is located at $x/c \approx 0.45$. Further increasing the Mach number yields a stronger shock oscillation with buffet onset starting approx. at $Ma = 0.73$. Moreover, we observe that the mean shock locations is shifted downstream with a higher Mach number. The corresponding probability density distributions given in Fig. 6b show this behaviour in a time-independent representation. One can note that the PDFs are shifted to higher x/c-values for higher Mach numbers while the standard deviation of the distributions increases which suggests that the range of the shock movement is increased similarly.

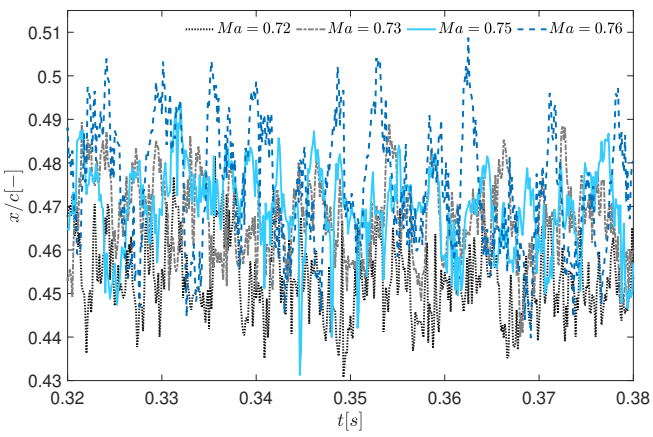

(a) Temporal extract of the instantaneous shock position for various Mach numbers

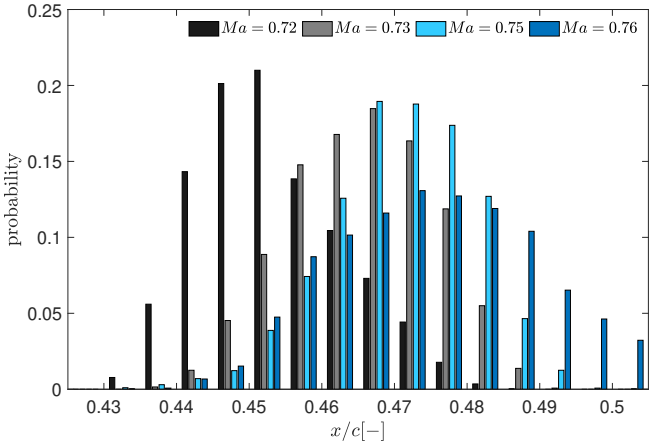

(b) PDF of the instantaneous shock position for various Mach numbers

Figure 6. Temporal extract of the instantaneous shock position and the corresponding PDF for various Mach numbers of the reference configuration. The higher the Mach number, the stronger the shock waves oscillate while the mean shock position shifts further downstream.

Fig. 7 captures the power spectra of an FFT applied to the instantaneous shock position for the investigated Mach number range side-by-side. In this figure, the absolute values of the FFT coefficients $|P|$ are squared and normalized by the signal length L to enable a comparison across different configurations. Only frequencies below $f = 1000Hz$ are shown since higher frequencies contain marginal power values. For $Ma = 0.72$, one can notice several peaks of equal strength. Overall, a slight buffet plateau becomes visible around $f \approx 200Hz$, but a distinct peak corresponding to transonic buffet is not detectable. This could be interpreted to indicate that this flow state represents a pre-buffet configuration. In contrast, a slight increase of the Mach number to $Ma = 0.73$ yields a distinct peak in the power spectrum proving that buffet is measured for this Ma number. Similarly, also frequencies in the vicinity of this peak increase. Similar observations can be made for higher Mach numbers. The strength of the buffet peak increases and is located at $f_{buffet} \approx 184Hz$. The general trend of a frequency band in the range of the buffet frequency remains detectable.

Next, we focus our attention on the properties of the boundary layer downstream of the shock wave as recent literature (Paladini, Beneddine, et al., 2019; Jiang et al., 2019; Paladini, Marquet, et al., 2019; D'Aguanno et al., 2021a,b) highlights the importance of this specific region. Fig. 8a depicts the probability density distribution of the streamwise and wall-normal velocity components for all six Mach number configurations within the separated boundary layer. For $Ma = 0.68$, one can observe high probabilities for comparably small streamwise velocity components ($0m/s \leq u \leq 75m/s$) followed by lower probabilities in the medium velocity range. The peak value at $u \approx 250m/s$ corresponds to the outer flow conditions at the boundary layer edge. Generally speaking, this PDF shape suggests that the boundary layer is characterized by partial flow separation. A systematic increase of the Mach number deforms this PDF in a way that the low velocity plateau is somewhat reduced and shifted to higher velocities. Moreover, recirculation within

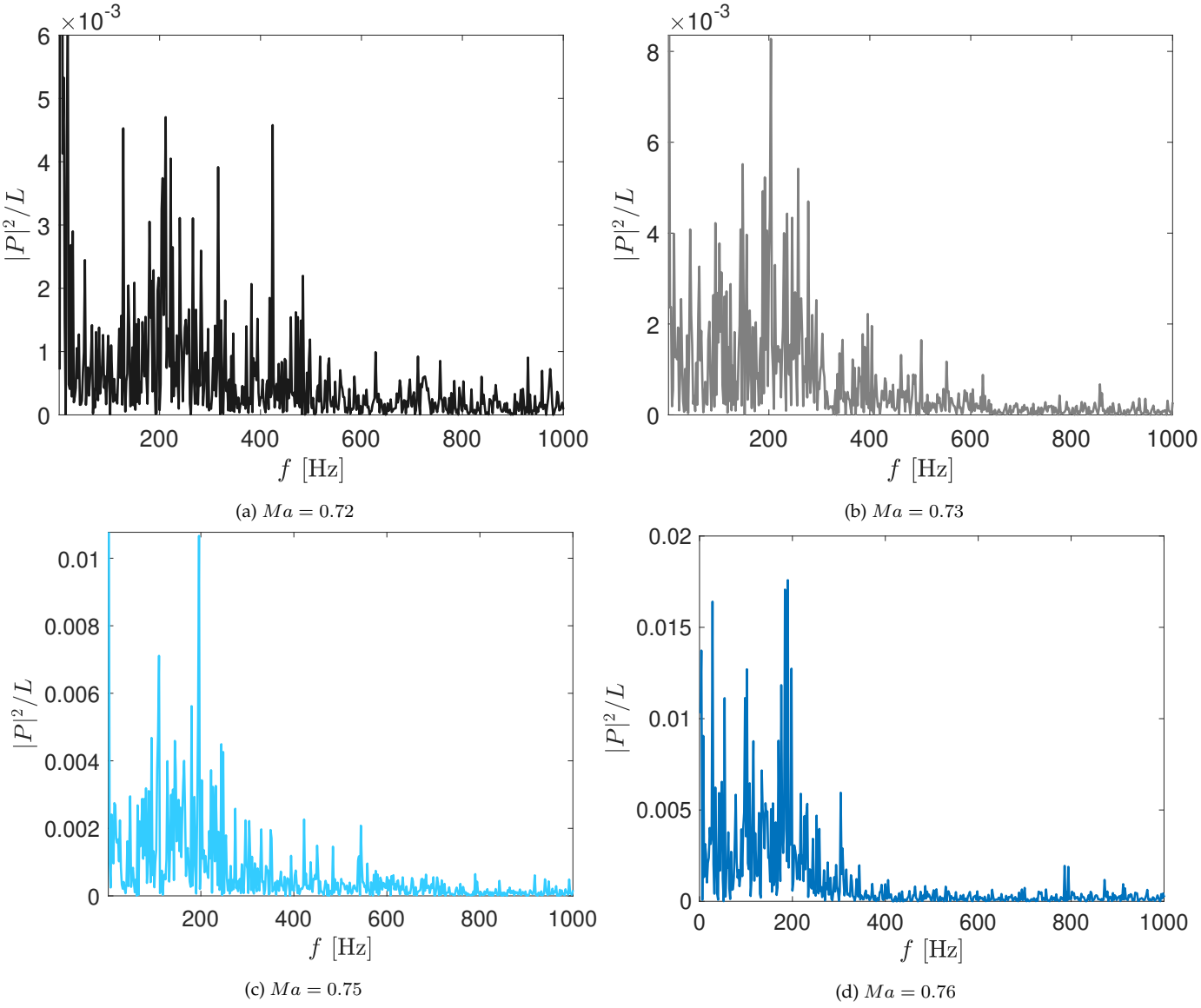

Figure 7. Power spectra of the FFT applied to the instantaneous shock position for various Mach numbers of the reference case.

the boundary layer is less probable indicating that the higher the Mach number becomes, the more the PDF is shifted towards a higher velocity range. In contrast, the wall-normal velocity distributions shown in Fig. 8b only vary slightly when systematically increasing the Mach number. In general, the overall trend can be summarized as follows: The higher the Mach number, the wider the respective PDFs and the lower the peak probabilities. These findings can be linked to the buffet typical "breathing" of the boundary layer inducing stronger absolute wall-normal velocities when the shock moves up- respectively downstream.

According to the feedback loop model of Lee (1990), pressure waves generated by the shock wave convect from the shock foot downstream within the boundary layer. When reaching the sharp trailing edge, strong acoustic waves are generated which in turn propagate upstream outside the boundary layer and interact with the shock foot to enhance its oscillatory motion. Improving this

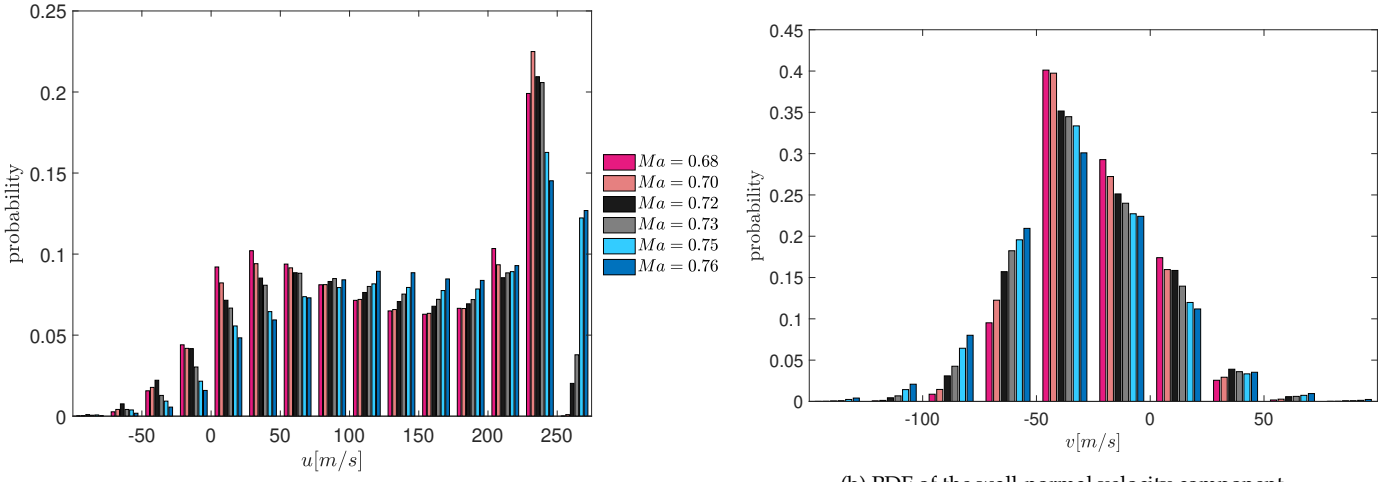

(a) PDF of the streamwise velocity component

(b) PDF of the wall-normal velocity component

Figure 8. Probability density distributions of streamwise (a) and wall-normal (b) velocity components of the boundary layer

model, Hartmann, Feldhusen, & Schröder (2013) suggest that the sound pressure level of these waves is modulated by the buffet frequency which might explain the self-sustained buffet characteristics. The essence of these buffet models builds upon a cause-effect relation between the shock movement, the boundary layer, and upstream traveling pressure waves and consequently forms some kind of feedback loop. Thus, we closely investigate the relevant flow structures, i.e., the upstream traveling waves (UTWs), in our BOS data, as these are suggested to be necessary for the interaction of the trailing edge and wake flow and the shock.

We employ an FFT to the flow data of the downstream positioned BOS camera (BOS camera 2 in Fig. 1) and reconstruct every frequency in the range $100Hz \leq f \leq 2500Hz$ individually applying an inverse FFT. Since we are only interested in the UTWs in the free flow field, the fixed data window is positioned far away from the boundary layer at any time and configuration. To determine if a specific frequency resembles UTWs, we cross-correlate consecutive, reconstructed snapshots, which yields the predominant direction of motion. Once all relevant frequencies are identified, we reconstruct the flow field using all frequencies corresponding to UTWs based on another inverse FFT. Note that the wave propagation direction of frequencies smaller or larger than the selected range cannot be tracked reliably. Thus, these frequencies are not used. However, the complete Fourier spectrum shows that these frequencies are not very relevant for the flow field since they possess small amplitudes and thus, it will not have a significant impact on the findings when they are neglected.

In a final step, we compute the spatial median of the squared reconstructed UTWs to obtain a 1D signal over time which gives a valuable intuition about the time-dependent overall sound pressure level. It allows the investigation how the strength of the UTWs varies with time and how these energy fluctuations relate to the shock movement. Note that in the following we denote this quantity sound pressure level. However, as we extracted it from density gradients captured in BOS data, this quantity should be understood as an approximation of the corresponding sound pressure level rather than an exact quantitative value. For the reference case, one can observe that the frequency

spectra of the UTWs is broadband and contains various frequencies of similar strength as depicted exemplary for the $Ma = 0.76$ test case in Fig. 9a. The power spectrum of the SPL further proves this initial impression since hardly any dominant peaks can be identified (see Fig. 9b).

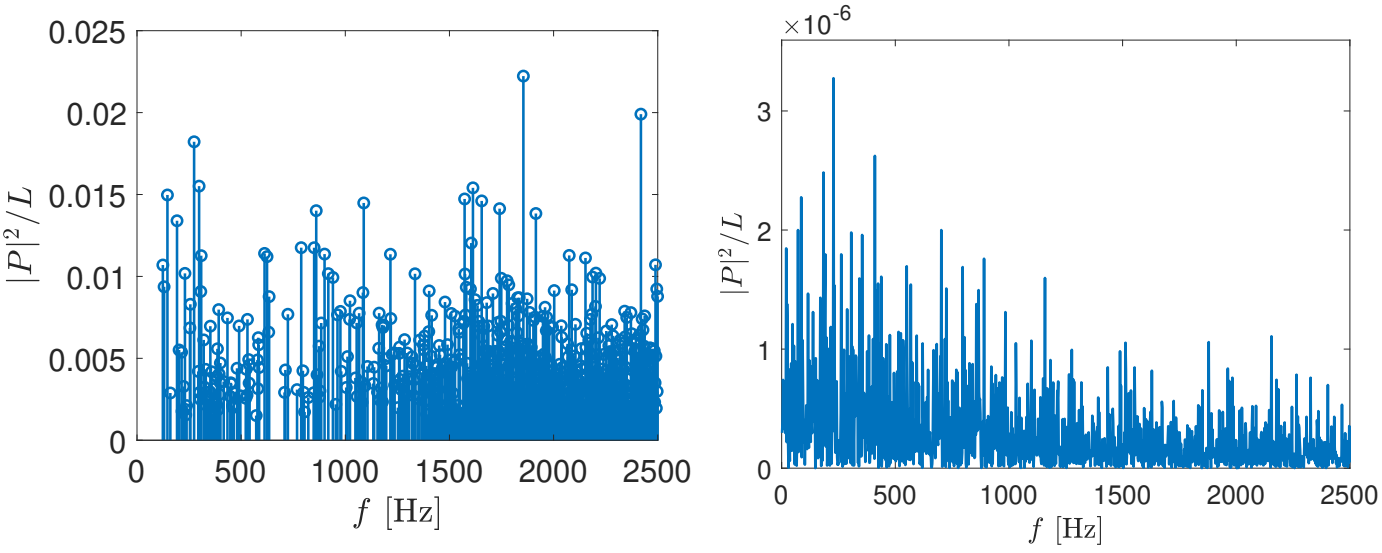

(a) Power spectra of the identified UTWs

(b) Power spectra of the SPL of the identified UTWs

Figure 9. Power spectra of the identified UTWs and their strength obtained by our BOS data for the reference test case at $Ma = 0.76$

4.3. External excitation of the transonic buffet flow using cavity noise

In this section, we particularly focus on the effect of artificial sound waves on transonic buffet to shed some light on the significance of upstream traveling pressure waves and their respective participation within the self-sustained shock oscillation. Thus, we perform extensive measurements in which we introduce artificial sound waves originating from the horn cavity and observe a strong buffet excitation. These acoustic modes resemble cavity-typical noise since the horn geometry represents a cavity to the surpassing flow. Thus, the shear layer originating from the upstream cavity edge interacts with the downstream cavity edge yielding some artificial noise. In this context, the horn acts as a resonator amplifying the cavity noise. To obtain a general insight in the acoustic modes related to the cavity noise, we perform reference measurements of an empty windtunnel configuration without an airfoil model installed. Fig. 10 depicts the FFT-based power spectra related to UTWs in the empty windtunnel configurations of both, the reference test case (cavity noise is suppressed by a perforated metal sheet) and the cavity noise configuration for $Ma = 0.76$. One can observe that the cavity noise comprises some peak frequencies in the range of $400Hz < f_{UTW} < 600Hz$ which are one order of magnitude stronger compared to the peak values of the reference configuration (see Fig. 10a). As the reference test case appears to be broadband without distinct peak values in this range, we conclude that the installation of the cavity modifies the characteristics of the UTWs significantly.

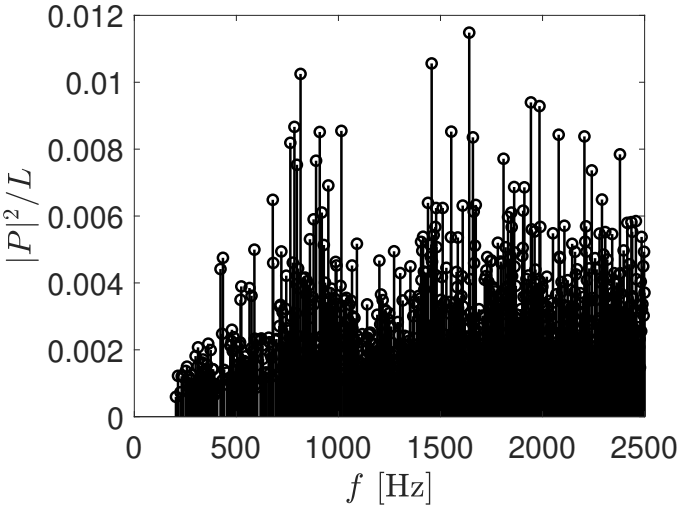

(a) Power spectra of the UTWs for an empty windtunnel configuration without external cavity noise at $Ma = 0.76$

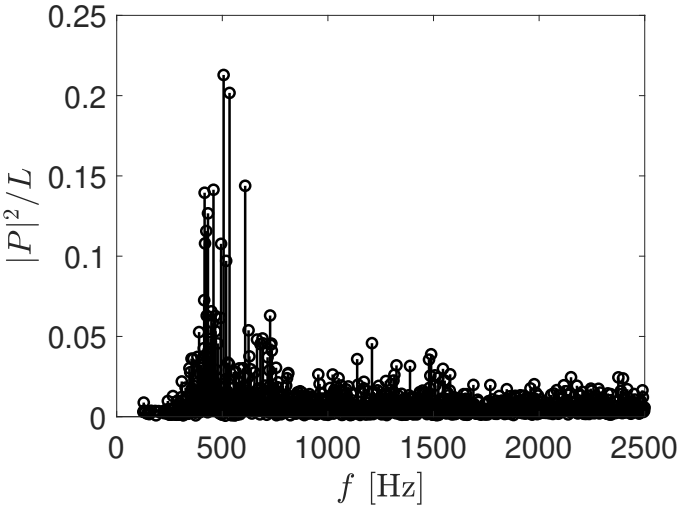

(b) Power spectra of the UTWs for an empty windtunnel configuration excited by external cavity noise at $Ma = 0.76$

Figure 10. Power spectra of the UTWs for an empty windtunnel configurations of the reference test case without cavity noise (a) and the cavity noise configuration (b) at $Ma = 0.76$

Thus, it is not surprising that this cavity noise influences the buffet characteristics of the transonic flow around the airfoil model substantially. Fig. 11a depicts the instantaneous shock position of this configuration (for brevity, it will be called CAV in the following) for fully developed buffet flow conditions at $Ma = 0.76$, which illustrate the substantial impact on the shock oscillation.

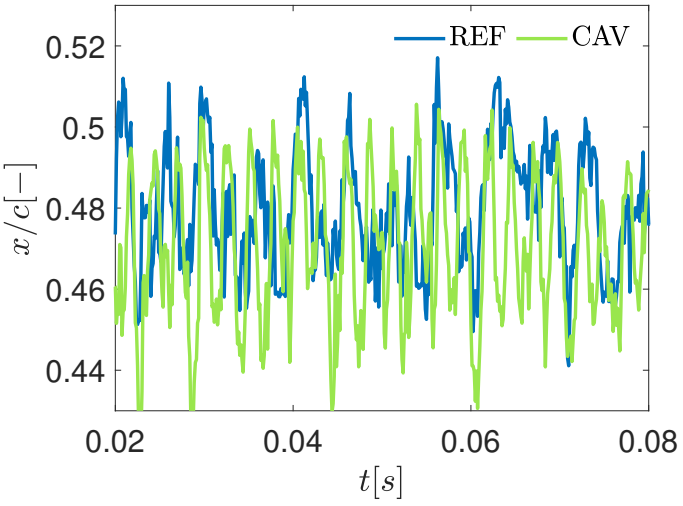

(a) Instantaneous shock position at $Ma = 0.76$

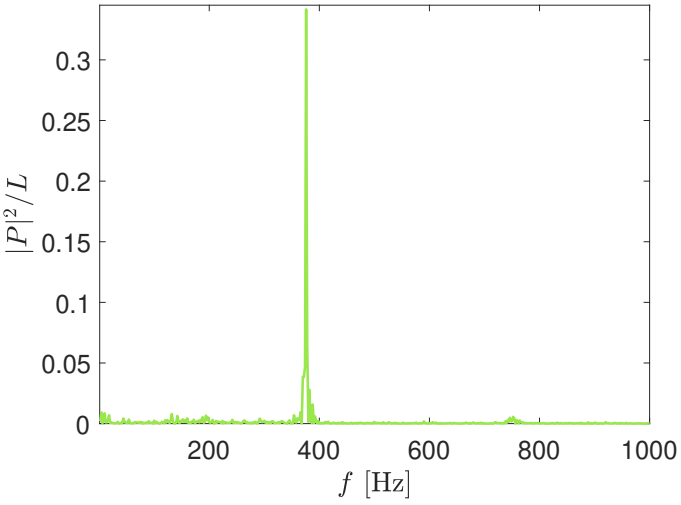

(b) Power spectra of the FFT applied to the instantaneous shock position at $Ma = 0.76$

Figure 11. Instantaneous shock position (a) and the corresponding FFT-based power spectra (b) for $Ma = 0.76$

One can observe that the amplitude of the shock movement is increased compared to the reference case ranging from $0.43 \leq x/c \leq 0.5$ and that the shock oscillation frequency increases substantially which is evidenced by a corresponding Fourier spectrum given in Fig. 11b. A single, distinct peak is visible which represents a new shock oscillation frequency of $f_{buffet} \approx 376Hz$. Further

note that the power of this peak is almost twenty times higher compared to the buffet peak of the reference case without cavity noise (see Fig. 7d) suggesting that the cavity substantially modifies the flow field and the shock oscillation. Complementary schlieren measurements revealed that the modified shock oscillation can be described as follows: The shock wave moves upstream until it reaches its most upstream position. Subsequently, the lower part of the shock remains at this location while the upper part bends forward until it breaks down. Afterwards, also the lower shock wave part starts dissolving in the most upstream position while a new shock wave is formed in the most downstream position. After its full development, it starts to move upstream and the cycle repeats. As a consequence, the shock movement no longer exhibits a sinusoidal motion and therefore, it does not satisfy the type A shock motion of Tijdeman (1977) anymore. More likely, one can connect our observation to the description of the type B motion which is characterized by an almost sinusoidal shock movement during which the shock wave partially disappears within its downstream excursion. In our cavity test case, however, the shock continuously disappears when moving downstream. In other words, our specific observations appear to be fundamentally different to any previously described transonic buffet flows over a DRA-2303 profile since the shock wave breaks down in its most upstream position and reforms further downstream. These findings evidence that the cavity noise, i.e., external noise sources, can strongly affect a transonic flow field. Hartmann et al. (2012) also noticed some external excitation when removing parts of the upper and lower windtunnel downstream of the airfoil. Thus, a cavity-like freestream-chamber noise is generated which interacts substantially with the flow field. It is suggested that this artificial sound source strongly excites the second harmonic of the buffet frequency since the observed shock oscillation frequency increases approximately by a factor of two from $f = 113Hz$ to $f = 248Hz$. A similar increase of the buffet frequency is also observed in the present study, but a direct link to the excitation of the second harmonic of the buffet instability is not possible. For instance, the results shown in Sec. 4.2 illustrate that the shock oscillation in the reference case is characterized by a frequency band (Fig. 7) which makes it difficult to identify a single frequency that we can connect to the first harmonic of the buffet phenomenon. If we assume an external excitation of this flow instability, we would expect that also the second harmonic should contain a specific frequency range. However, a distinct peak is observed for the fully developed buffet flow field (Fig. 11b).
However, we also note some major differences compared to Hartmann et al. (2012). For our CAV configurations, the strength of the external excitation increases the higher the Mach number becomes while Hartmann et al. (2012) report a decreasing influence of the freestream-chamber with increasing Mach number. Moreover, they describe the formation of an oblique shock system when the shock wave reaches its most upstream position. In the present study, the shock wave breaks down in its most upstream position and reforms further downstream. These differences most likely emanate from the different measurement setups.

To gain further insight in this interesting test case, we study the characteristics of the UTWs and show exemplary results for $Ma = 0.76$, but all findings similarly hold for lower Mach numbers. The resulting power spectra of an FFT applied to the UTWs as well as their sound pressure level is shown in Fig. 12. The identified UTWs are strongly dominated by a single peak of $f \approx 376Hz$

which is accompanied by its harmonics at $f = 752Hz$ and $f = 1128Hz$. The power spectra of the sound pressure level of these UTWs are similarly characterized by distinct peaks. One can identify a single, dominant peak at $f = 376Hz$ in the SPL of the $Ma = 0.76$ test case, which perfectly matches the observed buffet frequency. This evidences that the altered shock oscillation is the most important flow feature while naturally occurring shock oscillations in the range of $f_{buffet} \approx 180Hz$ are negligible since this frequency is neither observable in the shock movement nor in the UTW data. Moreover, these findings are in stark contrast to the results of the reference test case which is characterized by a rather broadband UTW frequency spectrum.

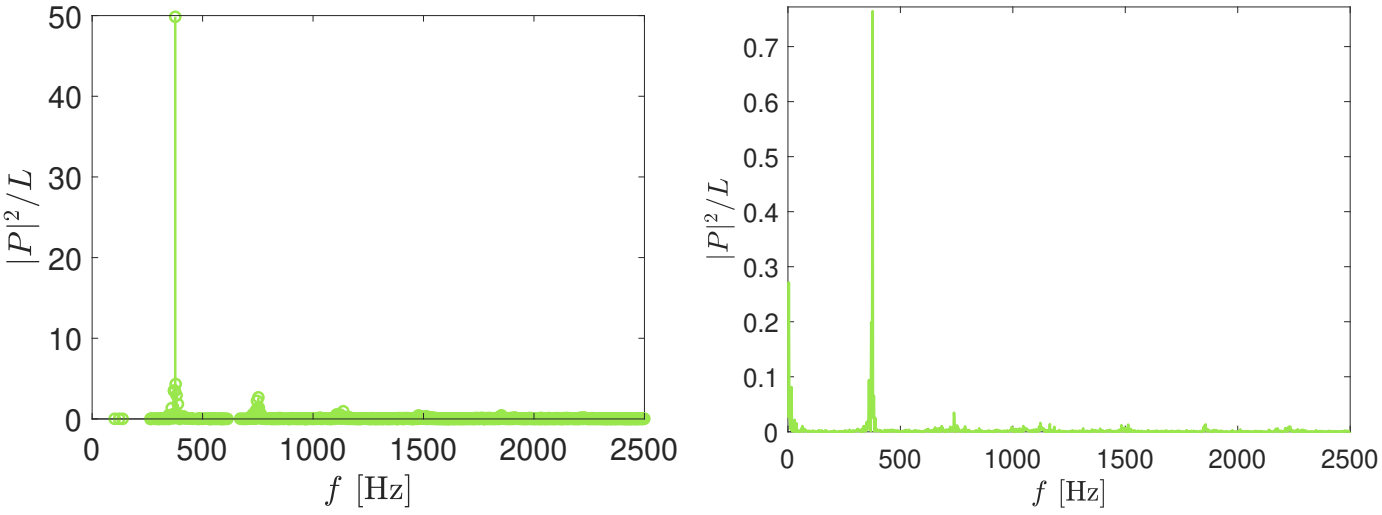

(a) Power spectra of the identified UTWs at $Ma = 0.76$

(b) Power spectra of the SPL of the identified UTWs at $Ma = 0.76$

Figure 12. Power spectra of the identified UTWs and their strength obtained by our BOS data for $Ma = 0.76$ altered by artificial cavity noise

5. Conclusions

Two fundamental goals motivate the present study: First, we intend to evidence the generalization and usefulness of our neural RAFT-PIV approach in challenging real-world applications and to enhance the general confidence in neural processing approaches amongst the experimental fluids community. Second, we focus on the significance of upstream traveling pressure waves and their respective participation within the self-sustained shock oscillation of transonic buffet.
Therefore, we employ our novel deep learning based RAFT-PIV approach to challenging real-world PIV and BOS measurements dealing with the transonic flow around a supercritical DRA-2303 airfoil. Overall, we evidence that RAFT-PIV can serve as a direct one-to-one replacement to traditional cross-correlation based PIV algorithms while effectively increasing the spatial output resolution. The extensive experiments further demonstrate that the proposed RAFT-PIV approach achieves state-of-the-art accuracy and generalization to new data, relative to both classical approaches and previously proposed optical flow learning schemes. RAFT-PIV is very robust to a range of common error sources and at least matches the performance of gold-standard PIV benchmark algorithms. The estimated displacements appear like realistic flow fields with sharp bound-

aries inbetween flow structures and a precise representation of small-scale structures.

The analysis of the importance of the UTWs can be summarized as follows. In the present investigation, transonic buffet becomes stronger with an increasing Mach number. The movement range of the shock comprises approx. $6\% - 8\%$ of the chord length and the oscillation frequency is approximately $f_{buffet} \approx 180Hz$. With increasing Mach number, we also observe variations in the streamwise velocity distribution within the boundary layer aft the shock wave. That is, a stronger recirculation is present in pre-buffet conditions, e.g., $Ma = 0.68$ or $Ma = 0.70$, which decreases with a higher Mach number. It appears that this is a characteristic for the large-scale shock oscillation of the DRA-2303 airfoil.
The findings of the cavity noise investigations evidence that it is indeed possible to trigger strong buffet-related shock oscillations and that the buffet frequency can be modified. The artificially introduced UTWs emitted by the cavity do not directly interact with the shock wave itself. The interaction is done by exciting the wake flow field that yields a modified buffet cycle. As a result, the buffet frequency shifts to $f = 376Hz$ while the shock movement increases. UTWs and shock oscillation frequencies in the range of the standard buffet phenomenon of the reference case cannot be detected meaning that the artificially triggered shock oscillation is the only dominating flow feature. In this context, we also detected UTWs at the new buffet frequency which are substantially stronger than any previously detected pressure waves.

Acknowledgements

This research was funded by the Deutsche Forschungsgemeinschaft within the research projects “Learning Deep Optical Flow Estimation for Particle-Image Velocimetry” (DFG SCHR 309/79) and "Experimental analysis of shock oscillations during shock-boundary layer interaction in transonic flow with artificially introduced sound waves" (KL 2138/5-1). The authors gratefully acknowledge the Gauss Centre for Supercomputing e.V. (www.gauss-centre.eu) for funding this project by providing computing time on the GCS Supercomputers HAWK at Höchstleistungsrechenzentrum Stuttgart (www.hlrs.de) and Juwels at the Forschungszentrum Jülich (www.fz-juelich.de).

References

Astarita, T., & Cardone, G. (2005). Analysis of interpolation schemes for image deformation methods in piv. *Experiments in fluids*, *38*(2), 233–243.

Crouch, J., Garbaruk, A., Magidov, D., & Travin, A. (2009). Origin of transonic buffet on aerofoils. *Journal of fluid mechanics*, *628*, 357–369.

D’Aguanno, A., Schrijer, F., & van Oudheusden, B. (2021b). Spanwise organization of upstream traveling waves in transonic buffet. *Physics of Fluids*, *33*(10), 106105.

D'Aguanno, A., Schrijer, F. F., & van Oudheusden, B. W. (2021a). Investigation of 3d shock control bumps for transonic buffet alleviation. In *Aiaa aviation 2021 forum* (p. 2558).

Deck, S. (2005). Numerical simulation of transonic buffet over a supercritical airfoil. *AIAA journal*, *43*(7), 1556–1566.

D'Aguanno, A., Schrijer, F., & van Oudheusden, B. (2019a). Study of upstream travelling waves in transonic buffet. In *Proceedings of the 13th international symposium on particle image velocimetry.*

D'Aguanno, A., Schrijer, F., & van Oudheusden, B. (2019b). Transonic buffet control by means of upper gurney flaps. In *Proceedings of the 54th international conference on applied aerodynamics (3af 2019).*

Feldhusen-Hoffmann, A., Statnikov, V., Klaas, M., & Schröder, W. (2018). Investigation of shock–acoustic-wave interaction in transonic flow. *Experiments in Fluids*, *59*(1), 1–13.

Hartmann, A., Feldhusen, A., & Schröder, W. (2013). On the interaction of shock waves and sound waves in transonic buffet flow. *Physics of Fluids*, *25*(2), 026101.

Hartmann, A., Klaas, M., & Schröder, W. (2012). Time-resolved stereo piv measurements of shock–boundary layer interaction on a supercritical airfoil. *Experiments in fluids*, *52*(3), 591–604.

Hartmann, A., Klaas, M., & Schröder, W. (2013). Coupled airfoil heave/pitch oscillations at buffet flow. *AIAA journal*, *51*(7), 1542–1552.

Huang, N. E., Shen, Z., Long, S. R., Wu, M. C., Shih, H. H., Zheng, Q., ... Liu, H. H. (1998). The empirical mode decomposition and the Hilbert spectrum for nonlinear and non-stationary time series analysis. *Proceedings of the Royal Society of London. Series A: Mathematical, Physical and Engineering Sciences*, *454*(1971), 903–995.

Jiang, R., Tian, Y., & Liu, P. (2019). Transonic buffet control by rearward buffet breather on supercritical airfoil and wing. *Aerospace Science and Technology*, *89*, 204–219.

Kojima, Y., Yeh, C.-A., Taira, K., & Kameda, M. (2020). Resolvent analysis on the origin of two-dimensional transonic buffet. *Journal of Fluid Mechanics*, *885*.

Lagemann, C., Lagemann, K., Mukherjee, S., & Schröder, W. (2021). Deep recurrent optical flow learning for particle image velocimetry data. *Nature Machine Intelligence*, *3*(7), 641–651.

Lagemann, C., Lagemann, K., Mukherjee, S., & Schröder, W. (2022). Generalization of deep recurrent optical flow estimation for particle-image velocimetry data. *Measurement Science and Technology*. Retrieved from `http://iopscience.iop.org/article/10.1088/1361-6501/ac73db`

Lee, B. (1990). Oscillatory shock motion caused by transonic shock boundary-layer interaction. *AIAA journal*, *28*(5), 942–944.

Marquardt, P., Klaas, M., & Schröder, W. (2019). Experimental Investigation of Isoenergetic Film-Cooling Flows with Shock Interaction. *AIAA Journal*, *57*(9), 3910–3923.

Mäteling, E., & Schröder, W. (2022). Analysis of spatiotemporal inner-outer large-scale interactions in turbulent channel flow by multivariate empirical mode decomposition. *Physical Review Fluids*, *7*(3), 034603.

Paladini, E., Beneddine, S., Dandois, J., Sipp, D., & Robinet, J.-C. (2019). Transonic buffet instability: From two-dimensional airfoils to three-dimensional swept wings. *Physical Review Fluids*, *4*(10), 103906.

Paladini, E., Marquet, O., Sipp, D., Robinet, J.-C., & Dandois, J. (2019). Various approaches to determine active regions in an unstable global mode: application to transonic buffet. *Journal of Fluid Mechanics*, *881*, 617–647.

Raffel, M., Willert, C., Scarano, F., Kähler, C., Wereley, S., & Kompenhans, J. (2018). *Particle image velocimetry: A practical guide, third edit.* Springer International Publishing AG.

Rehman, N., & Mandic, D. P. (2010). Multivariate empirical mode decomposition. *Proceedings of the Royal Society A: Mathematical, Physical and Engineering Sciences*, *466*(2117), 1291–1302.

Rehman, N., & Mandic, D. P. (2011). Filter bank property of multivariate empirical mode decomposition. *IEEE Transactions on Signal Processing*, *59*(5), 2421–2426.

Rehman, N., Park, C., Huang, N. E., & Mandic, D. P. (2013). EMD via MEMD: multivariate noise-aided computation of standard EMD. *Advances in Adaptive Data Analysis*, *5*(02), 1350007.

Sartor, F., Mettot, C., & Sipp, D. (2015). Stability, receptivity, and sensitivity analyses of buffeting transonic flow over a profile. *AIAA Journal*, *53*(7), 1980–1993.

Scarano, F. (2004). On the stability of iterative piv image interrogation methods. In *Proc. 12th int. symp. on appl. of laser techn. to fluid mechanics, lisbon, portugal.*

Siam, M., Valipour, S., Jagersand, M., & Ray, N. (2017). Convolutional gated recurrent networks for video segmentation. In *2017 ieee international conference on image processing (icip)* (pp. 3090–3094).

Teed, Z., & Deng, J. (2020). RAFT: Recurrent All-Pairs Field Transforms for Optical Flow. In *European conference on computer vision* (pp. 402–419).

Tijdeman, H. (1977). Investigations of the transonic flow around oscillating airfoils. *NLR-TR 77090 U*.

Tsai, R. (1987). A versatile camera calibration technique for high-accuracy 3d machine vision metrology using off-the-shelf tv cameras and lenses. *IEEE Journal on Robotics and Automation*, *3*(4), 323–344.

Westerweel, J., & Scarano, F. (2005). Universal outlier detection for piv data. *Experiments in fluids*, *39*(6), 1096–1100.

Xiao, Q., Tsai, H.-M., & Liu, F. (2006). Numerical study of transonic buffet on a supercritical airfoil. *AIAA journal*, *44*(3), 620–628.